X-ray Faraday rotation and magnetic circular dichroism in an iron-platinum compound

1999 J. Phys.: Condens. Matter 11 1159

(http://iopscience.iop.org/0953-8984/11/5/005)

J. Phys.: Condens. Matter **11** (1999) 1159–1175. Printed in the UK PII: S0953-8984(99)95587-X

X-ray Faraday rotation and magnetic circular dichroism in an iron–platinum compound

S P Collins
CLRC Daresbury Laboratory, Warrington WA4 4AD, UK

Received 3 July 1998, in final form 24 November 1998

Abstract. X-ray Faraday rotation—the dispersive analogue of x-ray magnetic circular dichroism—has been measured near the platinum L edges of ferromagnetic disordered Fe_3Pt using a simple new technique. We show that fractional x-ray intensity changes on magnetization reversal scale directly with the Faraday signal. The validity of the new approach as an alternative method for obtaining circular dichroism spectra is verified by performing simultaneous Faraday rotation and dichroism measurements, and comparing the results with Kramers–Kronig transforms.

1. Background

X-ray Faraday rotation (XFR) describes the tilting of a linearly polarized photon beam on passing through a magnetized medium, and is related at a fundamental level to x-ray magnetic circular dichroism (XMCD). In the latter—now the basis of a commonly used technique—the attenuation of a circularly polarized beam depends on the orientation of the sample's preferred magnetic axis with respect to the photon helicity. Alternatively, a linearly polarized beam, which can be considered as a coherent sum of left- and right-handed circular states, will emerge with elliptical polarization corresponding to the handedness of least attenuation. XFR is the dispersive analogue of XMCD in which the *phase velocity*, governed by the real part of the refractive index, depends on the sample's magnetization. One can think of the counter-rotating circular components of a linearly polarized beam oscillating at slightly different frequencies in the material, and emerging with a tilted electric vector.

Since absorption and dispersion are related through the Kramers–Kronig transform, it has been suggested and demonstrated [1] that XFR can be employed as an alternative to direct XMCD measurements for obtaining dichroic spectra, thus providing valuable information about the ground state of magnetic materials. Indeed, the quality of Faraday effect data was shown to compare favourably with that of circular dichroism. A strong argument in favour of the XFR technique is that it does not require a beam of circularly polarized x-rays. The key to the success of the first observations of XFR was a pair of tunable, ultrahigh-extinction-ratio x-ray polarizers [2]. Based on 'de-tunable' multi-bounce channel-cut silicon crystals, these novel devices provide the ultimate in sensitivity to small polarization changes over a moderately wide wavelength range. In this paper we explore the potential of using much simpler and more commonplace optical elements (a Si(111) channel-cut monochromator and a graphite analyser) to record similar data.

To appreciate the subtleties of XFR measurements it is useful to refer to figure 1, which illustrates the $\cos^2 \alpha$ intensity profile for a linearly polarized incident beam and a perfect linear

0953-8984/99/051159+17$19.50

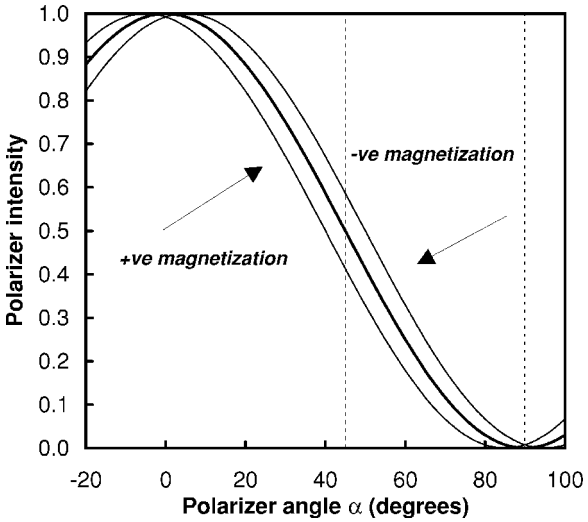

Figure 1. The effect of Faraday rotation on the intensity transmitted by a perfect linear polarization analyser. Two regions are of special interest: $\alpha \approx 90^\circ$ gives the largest fractional change of intensity with polarization rotation, as exemplified by Siddons *et al* [1], while $\alpha = 45^\circ$, employed for the present study, gives an intensity change which is nearly linear in the Faraday signal.

analyser. The 'crossed' setting with zero intensity occurs at an angle, α, which differs from 90° by the Faraday rotation angle, Ψ. The approach of Siddons *et al* [1] exploits the large enhancement in sensitivity to the Faraday signal very close to the crossed setting. Data taken over a range of angles were fitted to extract Ψ. Clearly, near-perfect polarizers are essential if the low beam intensity near $\alpha = 90^\circ$ is to be more strongly influenced by XFR than instrumental limitations. (In fact, even with perfect optics, the intensity does not generally drop to zero due to circular polarization induced by XMCD.)

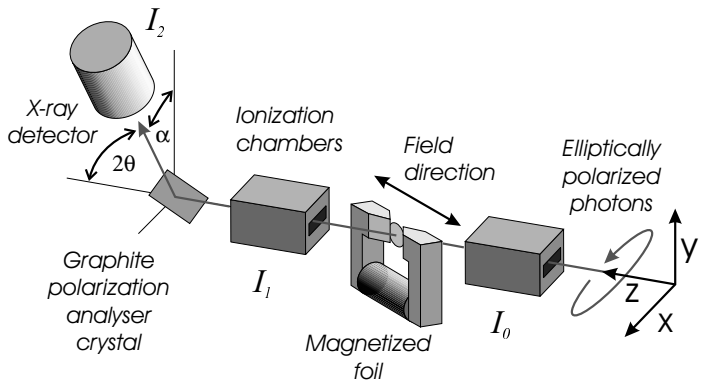

Figure 2. The layout for a combined XMCD and XFR experiment. As the magnetic field direction is reversed, modulations in the intensity ratios I_1/I_0 and I_2/I_1 scale with the XMCD and XFR strengths, respectively.

The present technique sets the polarization analyser to a fixed angle of $\alpha = 45^\circ$. Faraday rotation is then detectable as a relatively small intensity modulation when the magnetizing field is reversed periodically (see figure 1). While this approach lacks the inherent sensitivity of the

earlier work, it does offer some significant advantages. The fractional change in transmitted intensity scales *directly* with XFR, avoiding the need for re-positioning the analyser and curve fitting, and thus eliminating the associated systematic errors. Furthermore, the measured signal scales with the degree of linear polarization of the incident beam, and the *polarizance* of the polarization analyser—a number between zero and one that defines the sensitivity of the analyser to linear polarization. In the present set-up, imperfect optical elements have a modest, rather than catastrophic, effect on the data. The latter point allows for a very simple experiment (figure 2), which employs a graphite polarization analyser. In fact, virtually any analyser crystal will do; one simply adopts the Bragg reflection which occurs closest to $2\theta = 90^\circ$ in the energy range of interest. Moreover, since the incident linear polarization does not need to be very high, a beam of *elliptically* polarized photons can be employed. In that case, the Faraday signal is only marginally degraded, and one can determine simultaneously the XFR and XMCD spectra. Such a procedure, adopted here, is very useful for assessing the quality of the measured data, since each spectrum can be transformed into the other via a Kramers–Kronig transform.

2. Measurements on Fe_3Pt

To demonstrate this technique, we have studied the ferromagnetic Invar compound Fe_3Pt, measuring XMCD and XFR at the Pt L edges. Platinum $L_{2,3}$ dichroism signals in this and related compounds are known to be uncharacteristically large for hard x-ray resonances [3–9], and arise from dipole-allowed transitions from 2p core levels to the narrow Pt 5d band, polarized by the magnetic 3d metal ions, which appear as sharp 'white-line' features in the absorption spectra.

The measurements were performed on SRS Station 16.3, Daresbury Laboratory [10], using a Si(111) water-cooled channel-cut monochromator and no focusing elements. A fragment of an ingot of Invar Fe_3Pt, grown at the University of Birmingham, was cold rolled to form uniform foils (a procedure known to produce a disordered face-centred-cubic crystal structure [11, 6]), which were sandwiched between a pair of thin beryllium discs to prevent movement in the magnetic field. The sample foil, fixed between the poles of an electromagnet, was then mounted with two ionization chambers on the optics table, vertically translatable to allow polarization tuning [10], with a linear polarization analyser attached to the arm of the 16.3 diffractometer. While the diffractometer was not essential for the present study, its use allowed the Bede EDRa scintillation counter on the polarization stage to be separated by over two metres from the sample electromagnet—an essential precaution to ensure that the photomultiplier tube, even when wrapped in Mumetal foil, was completely unaffected by magnetic field modulations.

A suitable compromise between the degrees of circular and linear polarization in the incident beam, with both being around 70% in magnitude, required the source to be viewed at an angle of around 0.16 mrad above or below the plane of the electron's orbit. This was achieved with little loss of flux by translating the optics table and diffractometer by ± 5 mm. Measuring at the two positions provided a very sensitive test of systematic errors, since the XMCD signal should reverse sign with the photon helicity, while leaving the Faraday rotation unaffected. The only adjustment required when moving between the positive and negative helicity settings was a small correction to the x-ray energy calibration due to the change in beam angle with the monochromator.

The measurement sequence, orchestrated by the PINCER instrument control language and CLAM macro library [10], was as follows. For each absorption edge, the photon energy was scanned using a CLAM Virtual Motor (VM) macro to drive the monochromator and correct the graphite polarization analyser angle for the change in wavelength. A second VM then operated the sample electromagnet, reversing the 0.5 A current in an asynchronous $(+ - - + - + + -)$

Table 1. Some experimental parameters for the present study.

Beam to foil angle	45°
Magnetization projection $\|m_z\|$	0.707
Analyser angle (α)	45°
Vertical beam angle	0.155 mrad
Foil thickness	8 ± 1 μm

Table 2. The three polarization parameters (last three columns) relevant to the interpretation of the XFR and XMCD data.

Absorption edge	Energy (keV)	Graphite reflection	Analyser polarizance ($\sin^2 2\theta/[1+\cos^2 2\theta]$)	Linear polarization (P_3)	Circular polarization (P_2)
Pt L_3	11.564	(0, 0, 8)	0.935	0.70	$\pm$0.70
Pt L_2	13.273	(0, 0, 10)	0.998	0.69	$\pm$0.70
Pt L_1	13.880	(0, 0, 10)	0.974	0.69	$\pm$0.71

cycle (two seconds per position) and recording the integrated counts in all three x-ray detectors at each energy. Finally, in addition to the average transmitted intensity, two ratios were returned at each scan point:

$$R_1 = \frac{(I_1/I_0)_+ - (I_1/I_0)_-}{(I_1/I_0)_+ + (I_1/I_0)_-} \qquad R_2 = \frac{(I_2/I_1)_+ - (I_2/I_1)_-}{(I_2/I_1)_+ + (I_2/I_1)_-}$$

where $+/-$ refer to parallel/antiparallel coupling of the photon propagation vector and magnetization direction. The detectors to which the three intensities refer are illustrated in figure 2. Various parameters relevant to these measurements are given in tables 1 and 2.

Measurements performed at the Pt $L_{2,3}$ edges displayed, as expected, sizable XMCD and XFR. The signs of both spectra reversed between the L_3 and L_2 edges, reflecting the opposite spin–orbit coupling of the $2P_{1/2}$ (antiparallel) and $2P_{3/2}$ (parallel) core levels. Moreover, the XMCD data, unlike the Faraday signals, reversed with the photon circular polarization, all in accord with expectations (see the appendix). The only slight anomaly was the fact that the Faraday signal *did* change with helicity, slightly but reproducibly, particularly in the L_3-edge data (see figure 3). The reason for this is not clear, but the final Faraday spectrum was taken as the mean for the two helicity states on the grounds that this effect, which must depend on

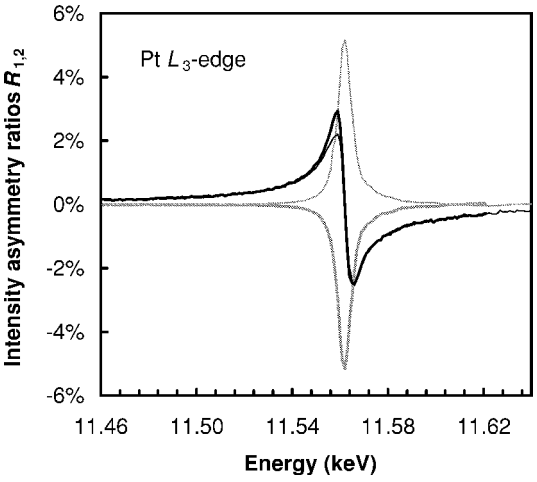

Figure 3. Raw intensity asymmetry ratios R_1 (grey) and R_2 (black) for the Pt L_3 edge. The thin curves correspond to positive helicity ($P_2 > 0$) and the thick curves to negative.

the circular polarization raised to an odd power, will then cancel.

Measurements were also made around the Pt L_1 edge, where the XMCD is extremely weak. As the Faraday signal at this edge was barely detectable above the statistical noise, the results are not reproduced here.

3. Data analysis

Detailed expressions for the intensity asymmetry ratios R_1 and R_2, caused by XMCD and XFR, respectively, are derived in the appendix, with the result

$$R_1 = P_2 \tanh(m_z\,\Delta\gamma\,t) \approx P_2 m_z\,\Delta\gamma\,t$$
$$R_2 \approx \left(\frac{\sin^2 2\theta}{1+\cos^2 2\theta}\right) P_3 m_z\,\Delta\gamma'\,t. \tag{1}$$

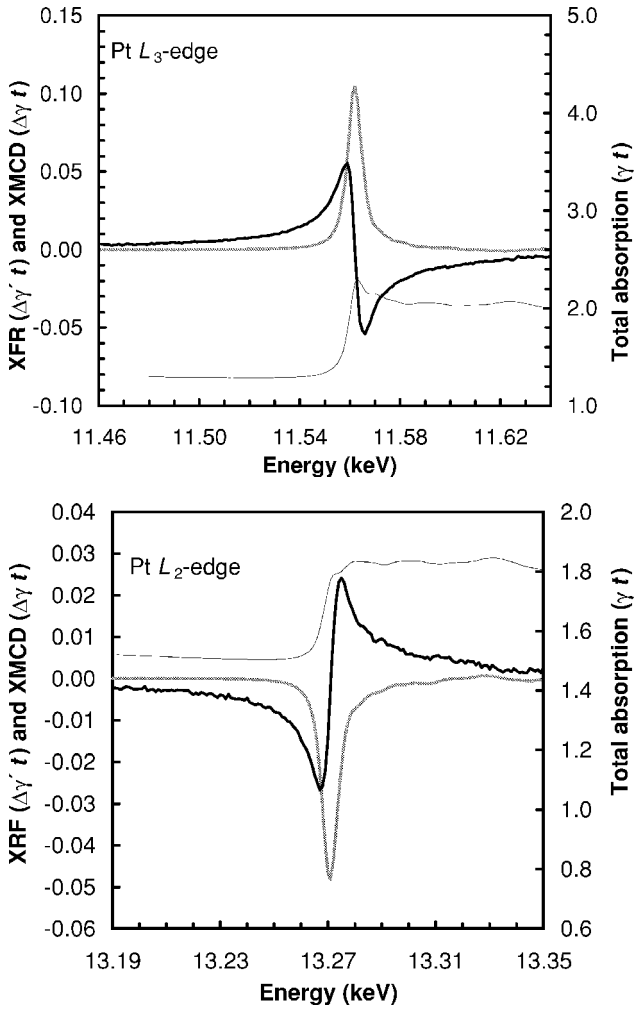

Figure 4. Contributions to the complex attenuation coefficient from Faraday rotation (black) and XMCD (grey), along with the total absorption (thin curve), near the platinum L_3 and L_2 edges.

Here, the quantities of interest are $\Delta\gamma$, the dichroic contribution to the linear absorption coefficient, and its dispersive analogue, $\Delta\gamma'$. For convenience we mainly consider the dimensionless products $\Delta\gamma\, t$ and $\Delta\gamma'\, t$, where t—the sample thickness—is given in table 1. In order to extract these quantities from experimental intensity ratios, one must possess accurate values for the Stokes parameters $P_{2,3}$, describing the degrees of circular and linear polarization in the incident beam, m_z, the projection of the magnetic quantization unit vector (assumed to be parallel to the external field) along the beam propagation direction, and θ, the polarization analyser Bragg angle. In fact, the latter two parameters are very easily determined (see tables), leaving the task of accurately determining the Stokes parameters as the key to quantitative data analysis. For the present work, the Stokes parameters were calculated using a program [12] which takes account of the synchrotron electron beam size and divergence. By far the largest uncertainties in the resulting Stokes parameters arise from errors in the vertical source parameters, chiefly the vertical electron beam divergence. Only after making several independent, and consistent, measurements of the relevant source parameters (see the appendix) were the computed Stokes parameters, reproduced in table 2, adopted with confidence.

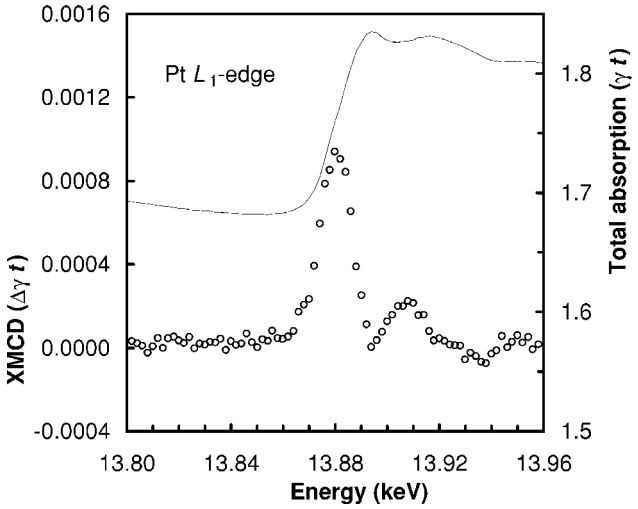

Figure 5. XMCD (circles) and total absorption near the platinum L_1 edge.

XMCD spectra for all three L edges, and the corresponding Faraday rotation spectra for the $L_{2,3}$ edges, are shown in figures 4 and 5, along with the total linear attenuation spectra. The results, particularly for the $L_{2,3}$-edge data, appear on inspection to be of very high quality. To *prove* that the spectra are quantitatively consistent requires further analysis, made possible because the reported measurements correspond to the absorptive and dispersive parts of the same complex response function: XMCD and XFR spectra are connected through the Kramers–Kronig transform [13]

$$\begin{aligned}\Delta\gamma'(E) &= \frac{2}{\pi}\mathrm{P}\int_0^\infty \frac{E'\,\Delta\gamma(E')}{(E'^2 - E^2)}\,\mathrm{d}E' \\ \Delta\gamma(E) &= -\frac{2}{\pi}E\,\mathrm{P}\int_0^\infty \frac{\Delta\gamma'(E')}{(E'^2 - E^2)}\,\mathrm{d}E'.\end{aligned} \tag{2}$$

In the above expressions, P represents the principal part of the integral, which excludes the pole at $E' = E$. Kramers–Kronig transforms are often rather difficult to compute since one needs to perform integrals over the *entire* energy spectrum, from zero to infinity. The present case

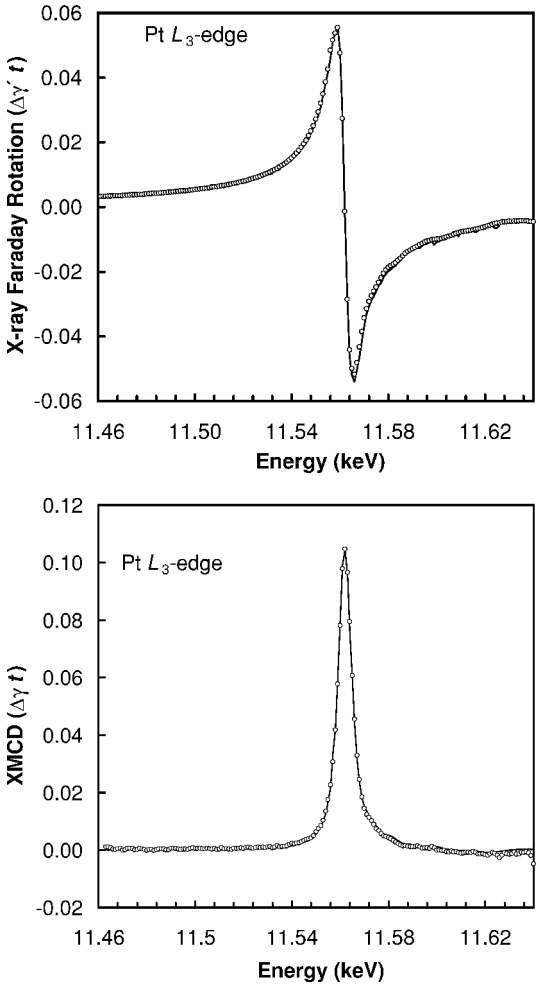

Figure 6. Top: platinum L_3-edge XFR (solid curve) along with the Kramers–Kronig transform of experimental XMCD data (circles). Bottom: the measured XMCD spectrum (solid curve) with the transform of the XFR measurements (circles) after applying the small correction described in the text.

is far more straightforward as we are only concerned with the dichroic part of the spectrum, which is only large in the vicinity of absorption edges. To apply these transformations to actual experimental data, one can replace the infinite integrals with finite summations to obtain the approximate expressions:

$$\begin{aligned}\Delta\gamma'(E) &\approx \frac{2}{\pi}\,\Delta E \sum_{E'=E_{\min}}^{E'=E_{\max}} \frac{E'(1-\delta_{E',E})}{(E'^{\,2}-E^2)+\delta_{E',E}}\Delta\gamma(E') \\ \Delta\gamma(E) &\approx -\frac{2}{\pi}E\,\Delta E \sum_{E'=E_{\min}}^{E'=E_{\max}} \frac{(1-\delta_{E',E})}{(E'^{\,2}-E^2)+\delta_{E',E}}\Delta\gamma'(E')\end{aligned} \tag{3}$$

where the Kronecker delta avoids infinities which contribute nothing in the original integrals. $E_{\min}$ and $E_{\max}$ represent the lowest and highest energies for which the spectra were measured, and it is assumed that the signals are zero outside of these limits. The result of applying

equations (3) to the measured XMCD data at the Pt L_3 edge, interpolated over a five-point spline to enhance the accuracy of the transform, is shown in figure 6. Agreement with the measured Faraday rotation spectrum, $\Delta\gamma' t$, is extremely good. Calculating the XMCD spectrum in a similar manner, however, produces a result which is not quite so impressive; while the central resonance is reproduced well, there is a marked divergence from the measured spectrum towards the edges.

The XFR results being harder to transform than the XMCD data can be attributed to the fact that, while the XMCD signals become vanishingly weak towards the edges of the spectral ranges, the Faraday signal does not (see figure 4). However, since there is very little spectroscopic fine structure in the tails of the Faraday rotation spectrum, it should be possible to calculate the effect of truncating the data. This can be achieved simply by assuming that the resonant tails approximate those of the *real* part of a single harmonic oscillator:

$$\Delta\gamma'(E) \approx \frac{A}{(E - E_0)} \tag{4}$$

where E_0 is the resonant centre and A is a constant which fixes the resonant amplitude. The correction to the Kramers–Kronig transform is then obtained by integrating this function from zero to infinity, but *excluding* the energy range covered by the measurements. One obtains

$$\begin{aligned}\Delta\gamma(E)_{\text{corr}} = {} & \frac{-2AE}{\pi}\left(\mathrm{P}\int_0^{E_1} \frac{1}{(E'^2 - E^2)(E' - E_0)}\,\mathrm{d}E'\right. \\ & \left. + \mathrm{P}\int_{E_2}^{\infty} \frac{1}{(E'^2 - E^2)(E' - E_0)}\,\mathrm{d}E'\right) \\ = {} & \frac{-A}{\pi(E^2 - E_0^2)}\{(E - E_0)\ln(E + E_1) + (E + E_0)\ln(E - E_1) \\ & - (E - E_0)\ln(E + E_2) - (E + E_0)\ln(E_2 - E) \\ & - 2E[\ln(E_0 - E_1) - \ln(E_2 - E_0) + \ln(E) - \ln(E_0)]\}. \end{aligned} \tag{5}$$

While this expression looks rather complicated, it relies on only two extra parameters, E_0 and A, both of which can be obtained by ensuring that the assumed form of the tails in equation (4) agrees with experimental Faraday rotation data near the edges of the spectrum. There are no freely adjustable parameters. After applying the above correction to the Kramers–Kronig transform, with $E_0 = 11.562$ keV and $A = -0.000\,31$, the measured XMCD spectrum is reproduced extremely well (figures 6 and 7).

The fact that each spectrum can be very accurately transformed into the other represents not just a proof of principle for the present technique, but also serves to validate the precise values for the Stokes parameters.

4. Discussion and conclusions

$L_{2,3}$-edge XMCD has been measured previously in iron–platinum compounds [3, 4, 6–9], and the present results appear to agree well with earlier findings. The spectra are dominated by a single strong resonance, attributed to $2p_{3/2,5/2}$–5d dipole-allowed transitions, where the narrow 5d band is polarized by the magnetic iron atoms. The L_2 resonance is around half the magnitude of the L_3 and of opposite sign, although it is around fifty per cent stronger than the L_3 peak when expressed as a fraction of the much smaller edge jump in the total linear attenuation coefficient.

An interesting question, yet to be resolved, arises from the difference in XFR signal (R_2) between measurements taken above the beam centre (positive helicity, P_2) and below (P_2

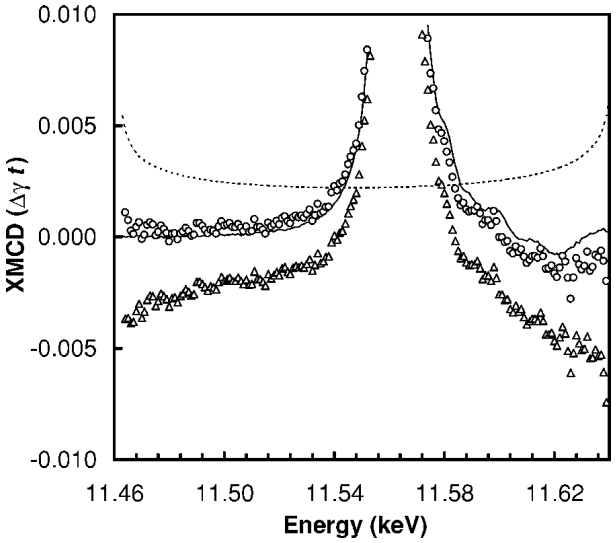

Figure 7. An expanded view of the platinum L_3-edge XMCD spectrum (solid curve) with the Kramers–Kronig transform of the measured XFR data. Triangles mark the uncorrected transform. When the correction (dotted curve) is added, agreement with the measured XMCD spectrum is improved dramatically (circles).

negative), as seen in figure 3. Since the XFR difference is outside of the scope of the present calculations, one or more of the model assumptions might be called into question. Two of these have been explored: a non-zero value of P_1 (the beam component polarized at 45° from the horizontal plane), and the presence of magnetic *linear* dichroism in the sample.

Repeating the calculations in the appendix, but without setting P_1 to zero, results in a modified series expansion for the intensity ratio in (A17):

$$R_2 = \left(\frac{\sin^2 2\theta \, m_z \{ P_3 \, \Delta\gamma' \, t + P_1 P_2 \, \Delta\gamma \, t \}}{1 + \cos^2 2\theta - P_1 \sin^2 2\theta} \right) + \mathrm{O}(t^3). \tag{6}$$

However, although P_1 does give a first-order correction to R_2, it is estimated that the polarization analyser would need to be misaligned by at least three degrees to account for the magnitude of the observed effect. This is at variance with detailed alignment checks carried out both above and below the beam centre. Moreover, the difference signal should scale with the dichroism spectrum $\Delta\gamma$, an almost symmetric function and quite different from the shape of the discrepancy, which is far more prominent on the low-energy side.

Calculations in the appendix have been extended to include magnetic *linear* dichroism (since the sample has a cubic crystal structure, there is no linear dichroism in the absence of magnetism). The results (equation (A27)) show that linear dichroism can contribute to second order in the ratios R_1 and R_2, and that there is a term in R_2 that reverses sign with the helicity. However, to account for the size of the XFR discrepancy, the linear and circular dichroism would need to be comparable in magnitude. This would seem highly unlikely for an ion with a moment that is far below saturation. Furthermore, if one includes the second-order terms then the two asymmetry ratios are not expected to be related by the Kramers–Kronig transform, which has been shown to apply very accurately with the present data.

The physical origin of the XFR discrepancy remains unclear, possibly arising in part from the above effects, plus perhaps non-uniformities in the sample thickness or errors in energy calibration between the measurements. However, the excellent agreement between

measurements and the results of Kramers–Kronig transforms is testimony to the reliability of the data after averaging for the opposite helicity states.

Results for the L_1 edge are far weaker than those at the $L_{2,3}$ edges, and have not, as far as we are aware, been reported before. Transitions from the 2s core level to the 5d band are forbidden by the dipole selection rules, while the dipole-allowed transitions probe only weakly polarized p bands. The result is therefore a very weak XMCD signal, which may arise from a combination of electric dipole and quadrupole transitions. Further measurements would be required to ascertain the multipole character of the spectrum.

While the weakness of the L_1 signal produced Faraday rotations which were below statistical noise levels, this was due to limitations in the present experimental set-up rather than the technique. In particular, the quality of the XFR data was sacrificed to enable simultaneous dichroism measurements. Without this requirement, the Faraday signal would be stronger, due to an increased linear polarization, and less noisy as a result of removing one ion chamber and moving to the beam centre. In addition to this, the peak reflectivity of the high-order graphite reflections used for polarization analysis was very low. Using an analyser crystal containing heavier elements should produce much higher count rates. A big advantage with the present technique is that almost any crystal can serve as an analyser, since the scattering angle does not need to be especially close to 90°. The sensitivity of the intensity modulation to the Faraday rotation could be enhanced by choosing an analyser angle, α, which is larger than 45° (i.e. closer to the 'crossed' setting). This approach may have some merit for studies of particularly small rotations, but it does become more sensitive to deficiencies in the beam polarization and polarization analyser. Moreover, the relationship between the intensity modulation, R_2, and the Faraday rotation becomes more complex and increasingly non-linear as $\alpha \rightarrow 90^\circ$.

The present study employed a beam of elliptically polarized x-rays in order to perform *simultaneous* XFR and XMCD measurements—the latter serving as a check on the former. The key question is: why not simply perform conventional XMCD measurement? Siddons *et al* [1] have argued that there are some intrinsic advantages in the XFR method. Moreover, it is shown in the appendix that for systems exhibiting both circular and linear dichroism, the second-order terms are not related through the Kramers–Kronig transform: the *combination* of XMCD and XFR spectra could then be used to separate the contributions from circular and linear dichroism. Perhaps the most obvious benefit of the Faraday rotation technique is that it can be performed with *linearly* polarized x-rays, sources of which are in abundance at synchrotron radiation centres. The added complexity of the present, fairly straightforward, approach must then be judged against techniques which measure XMCD by employing devices to convert from linear to elliptically polarized photons.

In summary, the essential difference between the present technique and previous approaches for monitoring the linear polarization of transmitted [1, 6, 14, 15] and diffracted [16, 17] beams is that we employ a fixed analyser angle and measure intensity modulations as the sample magnetization is reversed. We have shown that high-quality x-ray Faraday rotation data can be obtained with a very simple experiment. The recorded intensity modulations are shown theoretically to be almost linear in the XMCD and XFR coefficients. The quality of the data, validity of the technique, and precise values for the Stokes parameters are confirmed by the precision with which XMCD and XFR spectra can be interchanged via Kramers–Kronig transforms. We have demonstrated that a simple correction can be applied to the transform to account for the finite extent of the measured Faraday rotation spectrum. The fact that Kramers–Kronig transforms of localized resonant phenomena can be computed with such ease and accuracy should be of benefit to the interpretation of other types of experimental data, such as resonant magnetic scattering.

Acknowledgments

The author is grateful to D Fort and J S Abell, School of Metallurgy and Materials, University of Birmingham, for producing FePt ingots. Also, R Darlington for rolling sample foils, D Laundy for synchrotron beam calculations, and S W Lovesey for guidance on a number of theoretical aspects.

Appendix

A1. Magnetic circular dichroism with a partially polarized x-ray beam

The calculations performed here, based on polarization density matrices, employ the techniques and notation described in references [18, 19]. We begin by writing the density matrix for the incident beam in terms of the Stokes parameters:

$$\mu = \frac{1}{2}\begin{pmatrix} 1+P_3 & P_1 - \mathrm{i}P_2 \\ P_1 + \mathrm{i}P_2 & 1-P_3 \end{pmatrix} \tag{A1}$$

where $P_{1,2,3}$ are, respectively, the degrees of linear polarization at 45° from a plane of reference, mean helicity (circular polarization), and linear polarization within the plane. The polarization density matrix of a beam emerging from a medium is then

$$\mu' = A\mu A^{\dagger}/k \tag{A2}$$

where $k = \mathrm{Tr}(A\mu A^{\dagger})$ is the transmittance ratio (ratio of transmitted to incident intensity) and A is the transmission-amplitude matrix, whose elements represent the change in magnitude and phase of a pair of basis states, linearly polarized parallel and perpendicular to the plane of reference.

For a medium which exhibits circular dichroism (and no other polarization-dependent absorption) the transmission amplitude can be expressed very simply in terms of *circularly* polarized basis states:

$$A_c = \begin{pmatrix} \mathrm{e}^{\beta} & 0 \\ 0 & \mathrm{e}^{-\beta} \end{pmatrix} \tag{A3}$$

where $\beta = \frac{1}{2}m_z\,\Delta\tilde{\gamma}\,t$. Here, $\Delta\tilde{\gamma} = \Delta\gamma + \mathrm{i}\Delta\gamma'$ is the (complex) change in linear attenuation coefficient due to circular dichroism (the total attenuation is neglected for the present purposes as it does not affect the intensity *ratios*), m_z is the projection of the sample's magnetic symmetry axis (controlled by the direction of the applied magnetic field) along the photon propagation vector direction, and t is the sample thickness. The real and imaginary parts of the circular dichroism represent absorption and dispersion (responsible for Faraday rotation), respectively.

The next step is to convert the transmission matrix in (A3) to its equivalent form for linearly polarized basis states by writing

$$A = UA_cU^{\dagger} = \begin{pmatrix} \cosh\beta & -\mathrm{i}\sinh\beta \\ \mathrm{i}\sinh\beta & \cosh\beta \end{pmatrix} \tag{A4}$$

where the unitary matrix

$$U = \frac{1}{\sqrt{2}}\begin{pmatrix} 1 & 1 \\ \mathrm{i} & -\mathrm{i} \end{pmatrix} \tag{A5}$$

transforms from a circular to a linear representation of the polarization vectors.

Finally, by combining the above expressions, it is straightforward to compute the fractional change in transmittance upon reversing the magnetizing field direction:

$$R_1 = \frac{k(+m_z) - k(-m_z)}{k(+m_z) + k(-m_z)} = P_2 \tanh(m_z\,\Delta\gamma\,t). \tag{A6}$$

Two points are worthy of comment here. First, this result is identical to the operation of reversing the photon helicity and, secondly, the asymmetry ratio, R_1, depends only on the real (absorptive) part of the dichroism signal.

A2. Response of a diffracting linear polarization analyser

Linear polarization analysers, based on diffraction by imperfect crystals (kinematical diffraction), find use in a variety of x-ray experiments, including the present one. Here, we consider the relationship between relative intensities from a two-axis device and the photon beam polarization. Essentially, x-ray (charge) scattering alters the polarization of the beam because there is no field along the propagation direction (light is a transverse wave). Scattering means that the beam is deflected, and the field component along the new direction is lost. The scattering-amplitude matrix, which describes this polarization change, can therefore be computed simply by rotating to a coordinate system attached to the scattered beam and removing the field along the propagation direction.

The device adopted in this work, illustrated in figure 2, has two orthogonal rotation axes. The first rotates about the incident beam through an angle α. The second axis, attached to the first, causes the beam to be deflected by an angle 2θ. These operations are described by three-dimensional rotation matrices:

$$R_\alpha = \begin{pmatrix} \cos\alpha & -\sin\alpha & 0 \\ \sin\alpha & \cos\alpha & 0 \\ 0 & 0 & 1 \end{pmatrix} \qquad R_{2\theta} = \begin{pmatrix} 1 & 0 & 0 \\ 0 & \cos 2\theta & -\sin 2\theta \\ 0 & \sin 2\theta & \cos 2\theta \end{pmatrix}. \tag{A7}$$

Computing the scattering-amplitude matrix is then simply a matter of taking the upper-left four elements (transverse components) of the resultant transformation $R_{2\theta}R_\alpha$:

$$A_p = \begin{pmatrix} \cos\alpha & -\sin\alpha \\ \cos 2\theta \sin\alpha & \cos 2\theta \cos\alpha \end{pmatrix}. \tag{A8}$$

(It is worth noting that the scattering-amplitude matrix for any instrument can be computed using the above approach, which requires only the product of rotation matrices for each axis of the device.)

While there are many factors affecting the scattered intensity, we consider only those which depend on the polarization of the incident beam. The diffracted intensity is simply

$$\frac{I}{I_0} \propto \mathrm{Tr}(A_p \mu A_p^\dagger) \tag{A9}$$

which, evaluated in terms of Stokes parameters, leads to the result

$$\frac{I}{I_0} \propto \{P_3 \cos 2\alpha - P_1 \sin 2\alpha\} \sin^2 2\theta + \{1 + \cos^2 2\theta\}. \tag{A10}$$

This result, on which many experiments have been based, confirms that the polarization dependence of the analyser is greatest when $2\theta = 90^\circ$. It is also interesting to note that not only is the intensity independent of the helicity (P_2), but also it can be made independent of either P_1 or P_3 by making a suitable choice of the rotation angle α. A particularly simple case of equation (A10), where $2\theta = \alpha = 90^\circ$, is

$$I \propto I_0(1 - P_3) \tag{A11}$$

which is employed in this work to determine the effective beam divergence.

A3. Faraday rotation measurements

Having established the respective transmission- and scattering-amplitude matrices for a circular dichroic foil and linear polarization analyser, it becomes straightforward (in principle, at least!) to combine the two and describe the experiment depicted in figure 2. The relative intensity recorded by the third detector is simply

$$I_2 \propto \mathrm{Tr}(A_p A \mu A^\dagger A_p^\dagger) \tag{A12}$$

where A_p, A and μ are defined earlier in this appendix. What was a actually measured in the present study is the fractional change in *ratio* of intensity before and after the analyser as the magnetic field is reversed, namely,

$$R_2 = \frac{(I_2/I_1)_{m_z} - (I_2/I_1)_{-m_z}}{(I_2/I_1)_{m_z} + (I_2/I_1)_{-m_z}} \tag{A13}$$

where

$$\frac{I_2}{I_1} = \frac{\mathrm{Tr}(A_p A \mu A^\dagger A_p^\dagger)}{\mathrm{Tr}(A \mu A^\dagger)}. \tag{A14}$$

The result of a general evaluation of the above expressions is too cumbersome to be useful. However, certain limiting cases are manageable, and we begin by considering the instance where $\alpha = \pi/4$ and $P_2 = P_1 = 0$. The resulting asymmetry ratio reduces to

$$R_2 = P_3 \left(\frac{\sin^2 2\theta}{1 + \cos^2 2\theta} \right) \frac{\sin(m_z \, \Delta\gamma' \, t)}{\cosh(m_z \, \Delta\gamma \, t)}. \tag{A15}$$

Since there is no circular polarization in the incident beam, the signal vanishes as $\Delta\gamma' \to 0$. The first two factors merely represent the reduction in signal due to incomplete linear polarization (P_3) and the polarizance of the polarization analyser (see table 2). Setting these factors to unity (an ideal experiment) and assuming that the Faraday and XMCD signals are weak ($m_z \, \Delta\gamma' \, t, m_z \, \Delta\gamma \, t \ll 1$) leads to the particularly simple result

$$R_2 \approx m_z \, \Delta\gamma' \, t = 2\Psi \tag{A16}$$

where Ψ is the Faraday rotation angle. The experiment reported here was slightly more complex since, to facilitate simultaneous XMCD and Faraday measurements, the incident beam was elliptically polarized. As the exact result for R_2 in this case is very lengthy, it is useful to consider a series expansion in t which, for $P_1 = 0$ and an analyser angle of $\alpha = \pi/4$, begins

$$R_2 \approx \left(\frac{\sin^2 2\theta}{1 + \cos^2 2\theta} \right) P_3 m_z \, \Delta\gamma' \, t \left\{ 1 - \frac{(m_z \, \Delta\gamma \, t)^2}{2}(1 - 2P_2^2) - \frac{(m_z \, \Delta\gamma' \, t)^2}{6} \right.$$
$$\left. + \, P_2 P_3 (m_z \, \Delta\gamma \, t)(m_z \, \Delta\gamma' \, t) \left(\frac{\sin^2 2\theta}{1 + \cos^2 2\theta} \right) \right\} + \mathrm{O}(t^5). \tag{A17}$$

The first thing to notice about the above expression is the absence of even-order terms, since these do not change when the magnetic quantization vector is reversed. Even with the relatively strong XMCD/XFR signal in the present work, the third-order correction amounts to a fraction of a per cent. Moreover, after assigning appropriate values to the Stokes parameters, one finds that the largest of the third-order terms is the one which scales with $P_3^2 P_2$ and is eliminated by averaging measurements taken with left- and right-handed circular polarization.

To summarize, when the circular dichroism is modest (as is usually the case), one can reliably employ a first-order approximation to extract the Faraday rotation spectrum from experimental data, allowing a simple interpretation of the results of a simultaneous XMCD and XFR experiment.

A4. The transmission-amplitude matrix for more general cases

The transmission-amplitude matrix is determined by the exponential of a scattering operator. If one chooses basis states which are eigenstates of the operator, then they are also eigenstates of the exponential operator. The transmission-amplitude matrix then consists simply of diagonal exponential terms (see equation (A3) and reference [19]). While the 'trick' of adopting suitable basis states simplifies the calculations considerably, it becomes messy for more general physical systems.

In this section, we obtain an expression for the matrix elements $\langle\varepsilon'|\mathrm{e}^{\mathbf{S}}|\varepsilon\rangle$ (the form of a transmission-amplitude matrix) in terms of the scattering-amplitude matrix $\langle\varepsilon'|\mathbf{S}|\varepsilon\rangle$. The basis states are those of linear polarization along $\boldsymbol{x}$ and $\boldsymbol{y}$ (see figure 2), where the photon propagates along $\boldsymbol{z}$. A more detailed account of this procedure will be given in a subsequent publication [20]; here we reproduce some results which are of direct relevance to the present work.

To begin, write the matrix elements of the scattering operator

$$\langle\varepsilon'|\mathbf{S}|\varepsilon\rangle = \begin{pmatrix} S_{xx} & S_{xy} \\ S_{yx} & S_{yy} \end{pmatrix} \tag{A18}$$

as a linear combination of Pauli matrices [18]

$$\langle\varepsilon'|\mathbf{S}|\varepsilon\rangle = \beta\mathbf{I} + \boldsymbol{\alpha}\cdot\boldsymbol{\sigma} = \begin{pmatrix} \beta+\alpha_3 & \alpha_1 - \mathrm{i}\alpha_2 \\ \alpha_1 + \mathrm{i}\alpha_2 & \beta - \alpha_3 \end{pmatrix}. \tag{A19}$$

The advantage gained in employing Pauli matrices is soon apparent. By similarly writing the elements of $\mathrm{e}^{\mathbf{S}}$ as

$$\langle\varepsilon'|\mathrm{e}^{\mathbf{S}}|\varepsilon\rangle = \beta'\mathbf{I} + \boldsymbol{\alpha}'\cdot\boldsymbol{\sigma} \tag{A20}$$

one can exploit simple relationships between the matrix coefficients of the two operators [20]:

$$\begin{aligned} \beta' &= \mathrm{e}^{\beta}\cosh(\phi) \\ \boldsymbol{\alpha}' &= \boldsymbol{\alpha}\,\mathrm{e}^{\beta}\frac{\sinh(\phi)}{\phi} \\ \phi^2 &= \boldsymbol{\alpha}\cdot\boldsymbol{\alpha}. \end{aligned} \tag{A21}$$

It is then straightforward to map the matrix elements of $\mathrm{e}^{\mathbf{S}}$ onto those of $\mathbf{S}$, with the result

$$\langle\varepsilon'|\mathrm{e}^{\mathbf{S}}|\varepsilon\rangle = \mathrm{e}^{(S_{xx}+S_{yy})/2}\begin{pmatrix} \cosh(\phi) + \dfrac{S_{xx}-S_{yy}}{2}\dfrac{\sinh(\phi)}{\phi} & S_{xy}\dfrac{\sinh(\phi)}{\phi} \\ S_{yx}\dfrac{\sinh(\phi)}{\phi} & \cosh(\phi) - \dfrac{S_{xx}-S_{yy}}{2}\dfrac{\sinh(\phi)}{\phi} \end{pmatrix}$$
$$\phi = \sqrt{(S_{xx}+S_{yy})^2 + 4S_{xy}S_{yx}}. \tag{A22}$$

Using this general approach, one can take any scattering-amplitude matrix and compute the corresponding transmission amplitudes. The intensities from any experimental set-up involving transmission through a uniform medium can then be obtained using the procedures outlined in this appendix.

Example 1: circular dichroism/Faraday rotation

The scattering amplitude for a polarized atom exhibiting circular dichroism can be written as [18]

$$f_0 = a(\hat{\boldsymbol{\varepsilon}}'\cdot\hat{\boldsymbol{\varepsilon}}) + b\mathrm{i}(\hat{\boldsymbol{\varepsilon}}'\times\hat{\boldsymbol{\varepsilon}})\cdot\hat{\boldsymbol{m}} \tag{A23}$$

where $\hat{\boldsymbol{m}}$ is the unique magnetic symmetry axis, and a and b are complex resonant functions. The complex attenuation tensor can be written as

$$\tilde{\gamma} = \mathrm{i}\left(\frac{4\pi n_0}{q}\right) f_0 = A(\hat{\varepsilon}' \cdot \hat{\varepsilon}) + \mathrm{i}B(\hat{\varepsilon}' \times \hat{\varepsilon}) \cdot \hat{\boldsymbol{m}} \tag{A24}$$

where n_0 is the number of atoms per unit volume and q is the photon wavenumber ($q = 2\pi/\lambda$). From (A22) and (A24), one can write the transmission-amplitude matrix as

$$A = \langle \varepsilon' | \mathrm{e}^{-\tilde{\gamma} t/2} | \varepsilon \rangle = \mathrm{e}^{-At/2} \begin{pmatrix} \cosh(Bm_z t/2) & -\mathrm{i}\sinh(Bm_z t/2) \\ \mathrm{i}\sinh(Bm_z t/2) & \cosh(Bm_z t/2) \end{pmatrix} \tag{A25}$$

where t is the sample thickness. With $B = \Delta\tilde{\gamma}$, this is identical to the result (A4), obtained by using circular base states (the exponential pre-factor was omitted previously as it does not affect the polarization or intensity ratios).

Example 2: circular and linear magnetic dichroism

This is a slightly more complicated case, with a complex linear attenuation tensor of the form

$$\tilde{\gamma} = A(\hat{\varepsilon}' \cdot \hat{\varepsilon}) + \mathrm{i}B(\hat{\varepsilon}' \times \hat{\varepsilon}) \cdot \hat{\boldsymbol{m}} + C(3(\hat{\varepsilon}' \cdot \hat{\boldsymbol{m}})(\hat{\varepsilon} \cdot \hat{\boldsymbol{m}}) - (\hat{\varepsilon}' \cdot \hat{\varepsilon})) \tag{A26}$$

where C represents magnetic linear dichroism. One can readily obtain a general expression for the transmission-amplitude matrix, but for the purposes of the present work, we are more concerned with the special case where $m_x = m_z = 1/\sqrt{2}$, $m_y = 0$. On further assuming that $P_1 = 0, \alpha = \theta = \pi/4$ (which closely resembles the experimental situation), the two measured intensity asymmetry ratios reduce to

$$\begin{aligned} R_1 &\approx \frac{1}{\sqrt{2}} P_2 \,\mathrm{Re}\, B\, t - \frac{3}{4\sqrt{2}} P_2 P_3 \,\mathrm{Re}\, B \,\mathrm{Re}\, C\, t^2 + \mathrm{O}(t^3) \\ R_2 &\approx \frac{1}{\sqrt{2}} P_3 \,\mathrm{Im}\, B\, t + \frac{3}{4\sqrt{2}} P_2 P_3 \,\mathrm{Im}\, B \,\mathrm{Im}\, C\, t^2 \\ &\quad + \frac{3}{8\sqrt{2}} \{(1 - 2P_2^2) \,\mathrm{Re}\, B \,\mathrm{Im}\, C - (1 - 2P_3^2) \,\mathrm{Im}\, B \,\mathrm{Re}\, C\} t^2 + \mathrm{O}(t^3). \end{aligned} \tag{A27}$$

These expressions serve to highlight the possible influence of magnetic *linear* dichroism on the measured intensity ratios. Clearly, linear dichroism ($\mathrm{Re}\, C$ and $\mathrm{Im}\, C$) generates a number of second-order terms. The first-order terms remain unaffected.

It is interesting to note that there are two second-order terms in R_2 which require no polarization of the incident beam. Furthermore, the same two terms vanish for the case where $P_2^2 = P_3^2 = \frac{1}{2}$, which is very close to the present case. While the resulting expressions for R_1 and R_2 are pleasingly symmetric, only the first-order terms correspond to the real and imaginary parts of a spectral function: the second-order terms are not, in general, related through the Kramers–Kronig transform.

A5. Determination of the synchrotron electron beam divergence and photon Stokes parameters

The present data analysis relies on an accurate knowledge of the Stokes parameters for beams of elliptically polarized synchrotron radiation emitted at particular angles above or below the beam centre. These can be calculated by computing the flux and polarization profiles from an ideal (zero-emittance) source, and then convoluting the intensity-weighted Stokes parameters with functions—usually approximated by Gaussians—representing the appropriate (electron) source size and angular divergence. Since the two convolutions are equivalent to a single

broadening by an effective vertical source divergence parameter, $\sigma_{\rm eff}$, an accurate determination of this parameter is the key to characterizing the beam polarization. Here, five independent measurements have been combined to achieve a reliable value for the effective divergence parameter at Station 16.3, as summarized in table A1.

Table A1. Values for the effective synchrotron vertical beam divergence used to calculate Stokes parameters. The effective divergence includes a small contribution from the finite source size.

Method	$\sigma_{\rm eff}$ (mrad)
Horizontal polarization and flux profiles at 33.17 keV	0.040 ± 0.001
Vertically polarized intensity profile from PG (0, 0, 8) at 10.45 keV	0.039 ± 0.001
Vertically polarized intensity profile from PG (0, 0, 10) at 13.06 keV	0.038 ± 0.001
Total linear on-axis polarization at 10.45 keV	0.036 ± 0.001
Average of measured values	0.038 ± 0.001

First, the results of an analysis of the vertical intensity and linear polarization profiles measured with high-energy (33.17 keV) x-ray beams and a dichroic polarizer [19] were found to indicate a surprisingly low value of $\sigma_{\rm eff}$. To verify the high-energy result (the source divergence should be independent of the photon energy) two measurements of the height variation in the vertically polarized beam intensity (given by (A11)) were made using the polarization analyser described in this paper, with $2\theta = 90^\circ$, $\alpha = 90^\circ$, and the same pyrolytic graphite (PG) analyser crystal. The first of these employed the PG (0, 0, 8) Bragg reflection at 10.45 keV, and the second, the 13.06 keV PG (0, 0, 10) peak.

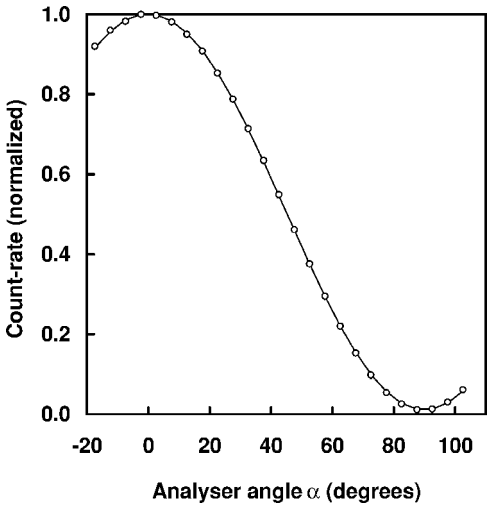

Figure A1. The variation in integrated diffraction intensity from the graphite (0, 0, 8) reflection of the linear polarization analyser at the beam centre (point of maximum linear polarization). The solid curve is a fit to a cosine-squared function.

The final measurement involved an absolute determination of the photon linear polarization at the point of maximum intensity, again using the PG (0, 0, 8) reflection at 10.45 keV, but this time taken with the rotation angle, α, varying form -15° to 105°. To ensure the reliability of these data, the analyser rocking curves were determined at each orientation, and the intensity taken as the background-subtracted peak areas. The result (figure A1) follows almost perfectly the cosine curve given in equation (A10), indicating a total on-axis beam polarization of

$P_3 = 0.978 \pm 0.001$.

The four values of σ_{eff}, extracted from five independent measurements (the intensity profiles are less sensitive than the other measurements and provide only confirmatory data) are in remarkably good agreement (see table A1), and therefore enable the circular and linear polarization parameters relevant to the present work to be calculated with confidence.

References

[1] Siddons D P, Hart M, Amemiya Y and Hastings J B 1990 *Phys. Rev. Lett.* **64** 1967
[2] Hart M and Rodrigues A R D 1979 *Phil. Mag.* B **40** 149
[3] Schütz G, Wienke R, Wilhelm W, Wagner W, Kienle P, Zeller R and Frahm R 1989 *Z. Phys.* B **75** 495
[4] Schütz G and Wienke R 1989 *Hyperfine Interact*. **50** 457
[5] Ebert H and Zeller R 1990 *Phys. Rev.* B **42** 2744
[6] Alp E E, Ramanathan M, Salem-Sugui S Jr, Oliver F, Stojanoff V and Siddons D P 1992 *Rev. Sci. Instrum.* **63** 1221
[7] Stähler S, Knülle M, Schütz G, Fischer P, Welzel-Gerth S and Buchholz B 1993 *J. Appl. Phys.* **73** 6063
[8] Baudelet F, Dubuisson J M, Hébert C, Créoff C, Pointal L, Andouard R, Odin S, Dartyge E, Krill G, Giorgetti C, Chervin J C, Itié J P, Polain A, Fontaine A, Pizzini S and Kappler J P 1998 *J. Synchrotron Radiat.* **5** 992
[9] Baudelet F, Odin S, Giorgetti Ch, Dartyge E, Itié J P, Polain A, Pizzini S, Fontaine A and Kappler J P 1997 *J. Physique Coll.* IV **7** C2 441
[10] Collins S P, Cernik R J, Fell B, Tang C C, Harris N W, Miller M C and Oszlanyi G 1998 *J. Synchrotron Radiat.* **5** 1263
[11] Wohlfarth E P and Buschow K H J 1988 *Ferromagnetic Materials* vol 4 (Amsterdam: North-Holland)
[12] Laundy D 1998 Private communication
[13] Jackson J D 1975 *Classical Electrodynamics* (Chichester: Wiley)
[14] Kortright J B, Rice M and Carr R 1995 *Phys. Rev.* B **51** 10 240
[15] Kortright J B, Kim S-K, Warwick T and Smith N V 1997 *Appl. Phys. Lett.* **71** 1446
[16] Gibbs D, Grübel G, Harshman D R, Isaacs E D, McWhan D B, Mills D and Vettier C 1991 *Phys. Rev.* B **43** 5663
[17] Mori K, Namikawa K, Funahashi Y, Higashi Y and Ando M 1993 *Rev. Sci. Instrum.* **64** 1825
[18] Lovesey S W and Collins S P 1996 *X-ray Scattering and Absorption by Magnetic Materials* (Oxford: Clarendon)
[19] Collins S P 1997 *Nucl. Instrum. Methods* B **129** 289
[20] Lovesey S W and Collins S P 1999 in preparation